Joule

Article

Competitive anion coordination overcomes charge-transfer barriers for lithium–sulfur batteries

Graphical abstract

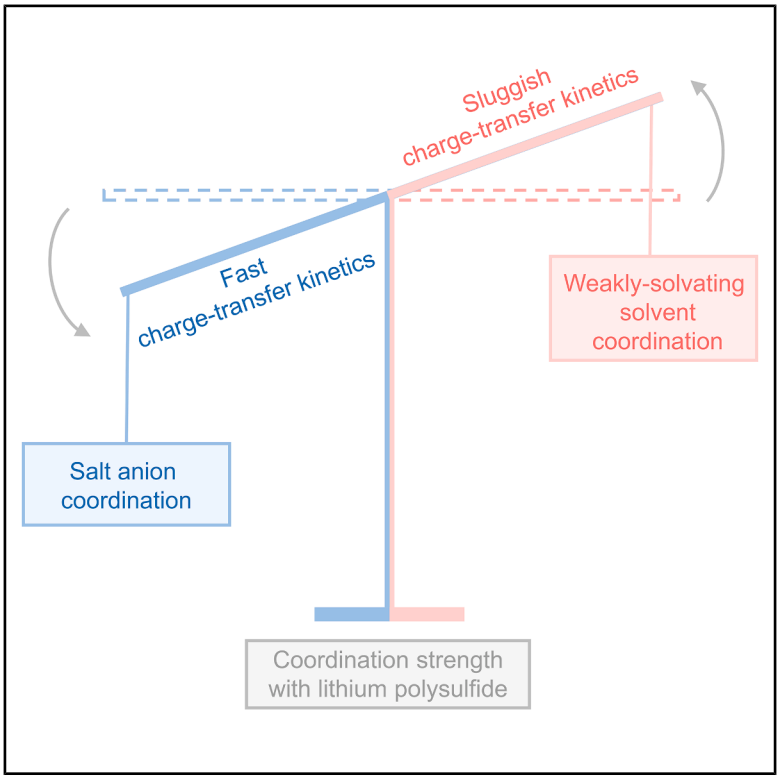

Authors

Xi-Yao Li, Bo-Quan Li, Tian Jin, ..., Xiang Chen, Jia-Qi Huang, Qiang Zhang

Correspondence

libq@bit.edu.cn (B.-Q.L.), zhang-qiang@mails.tsinghua.edu.cn (Q.Z.)

In brief

Anion-induced competitive solvation of lithium polysulfides (LiPSs) demonstrates a paradigm shift in advancing lithium–sulfur technology. The competition between anion and weakly solvating solvent coordination with LiPSs determines the charge-transfer kinetics. Strengthening anion coordination by using FSI^- promotes the LiPS kinetics and endows lithium-sulfur pouch cells with both high-energy-density and long cycling performances.

Highlights

- Revealing the competitive role of anions beyond conventional understanding
- Overcoming LiPS charge-transfer barriers via anion coordination
- Achieving record-breaking energy density in Ah-level pouch cells

Li et al., 2026, Joule *10*, 102259
February 18, 2026
https://doi.org/10.1016/j.joule.2025.102259

CellPress

Please cite this article in press as: Li et al., Competitive anion coordination overcomes charge-transfer barriers for lithium–sulfur batteries, Joule (2025), https://doi.org/10.1016/j.joule.2025.102259

Joule

CellPress

Article

Competitive anion coordination overcomes charge-transfer barriers for lithium–sulfur batteries

Xi-Yao Li,[1] Bo-Quan Li,[2,*] Tian Jin,[2] Shuai Feng,[3] Yu-Chen Gao,[1] Meng Zhao,[1] Xiang Chen,[1] Jia-Qi Huang,[2] and Qiang Zhang[1,4,5,6,*]

[1]Beijing Key Laboratory of Complex Solid State Batteries, Department of Chemical Engineering, Tsinghua University, Beijing 100084, China
[2]School of Interdisciplinary Science, Beijing Institute of Technology, Beijing 100081, China
[3]College of Chemistry and Chemical Engineering, Taishan University, Taian, Shandong 271021, China
[4]Institute for Carbon Neutrality, Tsinghua University, Beijing 100084, China
[5]State Key Laboratory of Chemical Engineering and Low-Carbon Technology, Tsinghua University, Beijing 100084, China
[6]Lead contact
*Correspondence: libq@bit.edu.cn (B.-Q.L.), zhang-qiang@mails.tsinghua.edu.cn (Q.Z.)
https://doi.org/10.1016/j.joule.2025.102259

CONTEXT & SCALE Lithium–sulfur (Li–S) batteries promise significantly higher energy densities than current lithium-ion technology. However, their practical implementation is hampered by sluggish lithium polysulfide (LiPS) kinetics. Though lithium salt anions are known for ionic conduction and interphase formation, their deeper influence on LiPS behaviors remains unexplored.

This work reveals a previously overlooked mechanism where anions compete with weakly solvating solvent to coordinate LiPSs. By strategically enhancing anion coordination, the sluggish LiPS charge-transfer kinetics are dramatically accelerated. The kinetic breakthrough enables practical 10-Ah-level pouch cells achieving a state-of-the-art 622 Wh kg^{-1} (based on total weight) with stable cycles. Moving beyond conventional anion roles, our findings establish a new design principle for developing ultrahigh-energy-density Li–S batteries.

SUMMARY

Beyond ionic conduction and solid-electrolyte interphase formation, the fundamental roles of lithium salt anions in batteries remain unexplored. Herein, an anion-induced competitive solvation mechanism that governs lithium polysulfide (LiPS) behaviors in high-energy-density lithium–sulfur batteries is pioneeringly unveiled. Specifically, anions contend against weakly solvating solvents to occupy the LiPS inner solvation shell. Enhancing anion coordination while diminishing weakly solvating solvent coordination overcomes the rate-determining LiPS charge-transfer barriers. As a proof of concept, bis(fluorosulfonyl)imide anion coordination reduces activation polarization and boosts cycling stability at high current densities. Ah-level pouch cells achieve stable operation at high rates of 0.35 C and deliver a record-setting energy density of 622 Wh kg^{-1} (based on total weight) with stable cycling. By elucidating the anion-induced competitive solvation mechanism, our work transcends conventional views of anion roles and establishes a new paradigm for advancing practical Li–S batteries.

INTRODUCTION

Salts play fundamental and irreplaceable roles in batteries.[1–4] They are dissociated into cations and anions to afford ionic conductivity of electrolyte and maintain stable operation of batteries.[5–8] Salt cations are generally solvated by solvents, and their behaviors have been extensively elucidated in previous researches.[9–12] In contrast, the role of salt anions is always overlooked, especially in affecting the electrode kinetics.[13–15] This oversight is more critical in conversion-type electrode systems, which offer high energy densities but involve soluble active intermediates coexisting with anions in the electrolyte. Under operational conditions, inevitable interactions occur between intermediates and anions, affecting both thermodynamics and kinetics.[16–19] Previous studies noticed anion alteration impacts electrode kinetics and performance, yet molecular-level mechanisms remain a mystery.[20,21] Therefore, elucidating the role of salt anions in modulating the electrode kinetics is essential to

Please cite this article in press as: Li et al., Competitive anion coordination overcomes charge-transfer barriers for lithium–sulfur batteries, Joule (2025), https://doi.org/10.1016/j.joule.2025.102259

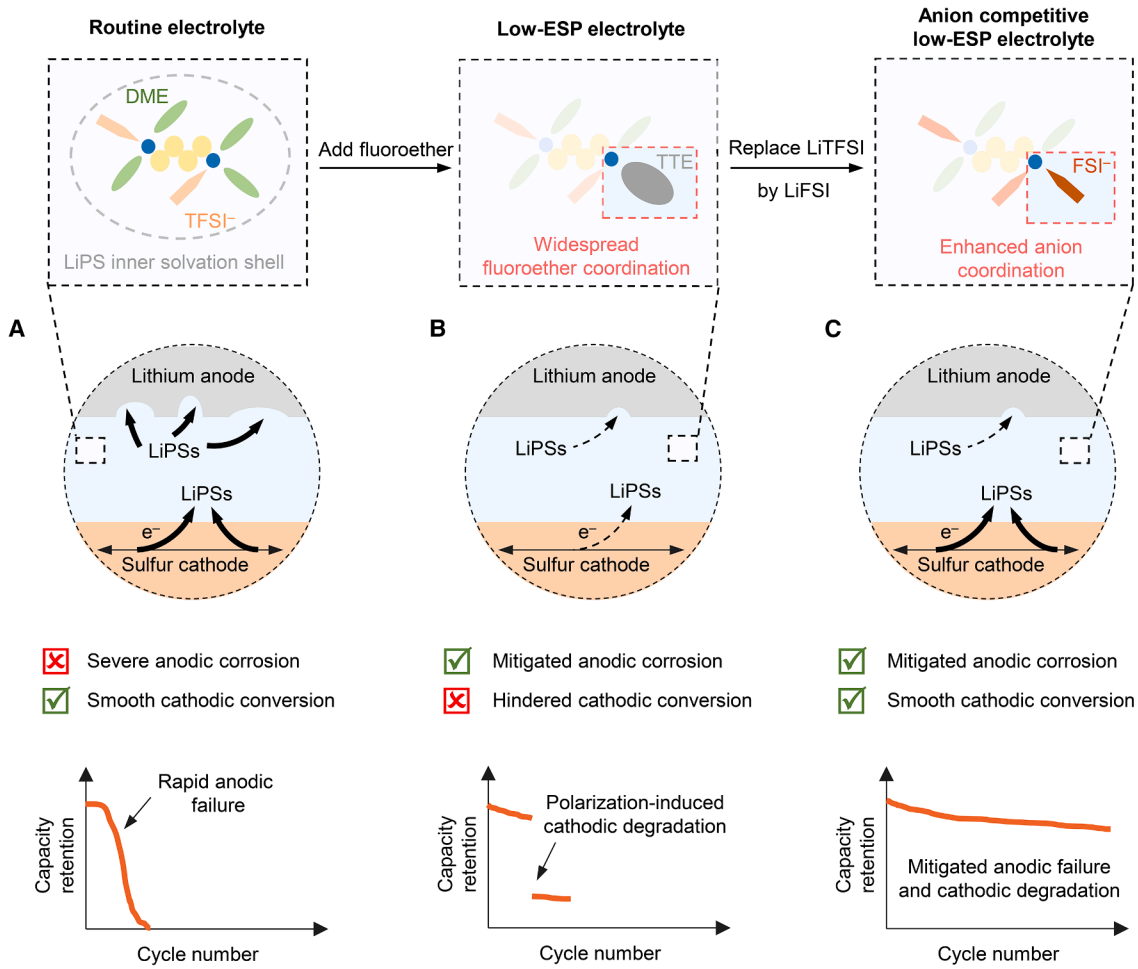

Figure 1. Schematic diagram of the LiPS behaviors in electrolytes through anion regulation

(A–C) Scheme of LiPS solvation shell evolution (1st line), anodic and cathodic behaviors (2nd line), and full-cell performances (3rd line) in (A) routine electrolyte, (B) low-ESP electrolyte, and (C) anion-competitive low-ESP electrolytes.

understand the electrode and electrolyte behaviors and realize high-performance batteries.

Elemental sulfur (S_8) is a representative conversion-type cathode material.[22–25] Paired with lithium-metal anodes, lithium–sulfur (Li–S) batteries promise an ultrahigh theoretical energy density of 2,600 Wh kg^{-1}. S_8 undergoes stepwise redox reactions, generating soluble lithium polysulfides (LiPSs) and ultimately solid lithium sulfide (Li_2S).[26–29] Therein, LiPSs serve as key intermediates determining the cathodic and anodic behaviors through bypassing the direct solid-solid conversion kinetic limitations in the cathodic compartment, while corroding the lithium metal and causing rapid anodic degradation.[30–33] Previous works have demonstrated that the LiPS reactivity can be reduced in low electrolyte solvating power (ESP) conditions, resulting in mitigated anodic parasitic reactions and promoted Li–S battery cycling performances.[34,35] Typically, the ESP can be altered by introducing fluoroether or other weakly solvating solvents as the regulator.[36–38]In electrolytes with relatively low ESP, though the lithium-metal anode stability can be greatly enhanced, the non-negligible cathodic polarizations and capacity loss induced by the impaired LiPS kinetics arise simultaneously, especially under high rates[39–41] (Figures 1A and 1B). Therefore, enhancing the LiPS cathodic kinetics in low-ESP electrolytes is crucial for achieving superior anode and cathode performances currently in Li–S batteries. In the low-ESP electrolytes with fixed solvent composition, tuning salt anions offers a potential route to alter the LiPS cathodic kinetics, warranting investigation into the underlying molecular-level mechanism.

In this contribution, an anion-induced competitive solvation mechanism for LiPSs is pioneeringly disclosed to accelerate the LiPS kinetics. Similar to solvents, salt anions can participate in the LiPS inner solvation shell, directly coordinating with LiPSs via lithium bonding.[42] Crucially, anions contend against fluoroether for entering the LiPS inner solvation shell, and the anion proportion is determined by its competitive solvation capability (Figure S1). Strengthening anion coordination and diminishing fluoroether coordination accelerates the charge-transfer kinetics governing LiPS homogeneous and heterogeneous reactions. As a proof of concept, bis(fluorosulfonyl)imide anion (FSI^-) coordination exhibits superior capability in contending against

Please cite this article in press as: Li et al., Competitive anion coordination overcomes charge-transfer barriers for lithium–sulfur batteries, Joule (2025), https://doi.org/10.1016/j.joule.2025.102259

fluoroether compared with bis(trifluoromethanesulfonyl)imide anions ($TFSI^-$) (Figure 1C). Consequently, LiPSs coordinated by FSI^- intrinsically possess faster charge-transfer kinetics. Adopting LiFSI as the lithium salt successfully addresses the sluggish cathodic kinetics and endows Li–S batteries with reduced activation polarization and promoted cycling stability at high rates. Furthermore, 10-Ah-level Li–S pouch cells employing the anion-induced competitive solvation approach achieve an ultrahigh energy density of 622 Wh kg^{-1} (based on total weight) with stable cycling.

RESULTS

Kinetic evaluations with distinct anions in electrolytes

1,1,2,2-tetrafluoroethyl-2,2,3,3-tetrafluoropropylether (TTE) serves as a representative regulator to lower ESP due to the steric-hinderance and the electron-withdrawn effect of the fluoroalkyl groups adjacent to the coordinating oxygen atom. 1,2-dimethoxyethane (DME) is a typical strongly solvating solvent to form stable five-membered-ring chelates. Mixing TTE and DME with variable contents can dynamically alter the ESP. Experimentally, the ESP can be quantitatively reflected by the Gutmann donor number (DN), and the measured DN is indeed decreased by 0.3 kcal mol^{-1} with the increment of the TTE content from 0% to 40% (Figures S2–S4). The reduced DN values illustrate that the ESP can be effectively regulated by tuning the TTE content in the electrolytes.

For the anodic behavior evaluations, the shuttle current gets lowered from 0.070 to 0.029 mA at 2.37 V as the ESP gets lowered. The Coulombic efficiency is promoted from 22.1% to 84.2% when the TTE content rises from 0% to 40% (Figures S5 and S6). The reduced shuttle current and promoted Coulombic efficiency manifest that the reducing ESP can mitigate the parasitic reactions between LiPSs and the lithium-metal anode. The above issues are attributed to tighter TTE encapsulation for LiPS solvation, rendering a lower ESP and reduced LiPS reactivity. From the anodic aspect, it is believed that the cycling stability of Li–S batteries can be better if the ESP gets weaker.

For the cathodic behavior evaluations, rate performances from 0.1 to 0.5 C with variable TTE content (from 0% to 40%) LiFSI/LiTFSI-based electrolytes are evaluated in Li–S full cells with high-sulfur-loading (4.0 mg_S cm^{-2}) cathodes (Figures 2A, 2B, S7 and, S8). In LiTFSI-based electrolytes, the cathodic kinetics are impaired with reduced ESP under a fixed discharge rate. For instance, the lowest discharge voltage ($U_{Dis\text{-}lowest}$, defined in Table S1) reduces from 1.99 to 1.82 V under 0.3 C, and the specific capacity drops from 821 to 693 mAh g^{-1} when the TTE content alters from 0% to 40% in LiTFSI-based electrolytes (Figures $2A_1$ and S7). Additionally, the polarizations are enlarged and specific capacities are reduced as the discharge rate increases in all electrolytes. Taking the cell with LiTFSI-based 20% TTE electrolytes as an example, along with the rate increased from 0.1 to 0.5 C, the $U_{Dis\text{-}lowest}$ reduces from 2.06 to 1.77 V, and the specific capacity drops from 908 to 673 mAh g^{-1} simultaneously (Figures $2A_2$ and S7). Moreover, the combination of low-ESP electrolytes and high rate (e.g., cells with 40% TTE electrolytes under 0.5 C, the upper-right corner in Figure 2A) can be the harshest condition for the cathodic kinetics regarding polarizations and specific capacities. In LiTFSI-based electrolytes with over 30% TTE, $U_{Dis\text{-}lowest}$ falls below the discharge cut-off voltage of 1.7 V under 0.5 C, eliminating the 2nd discharge plateau and causing over 60% specific capacity loss (Figure S7). Therefore, unbearable polarization hinders normal operation of Li–S batteries with low-ESP LiTFSI-based electrolytes under high rates.

The unbearable polarization issues in Li–S batteries with low-ESP electrolytes can be alleviated after replacing LiTFSI with LiFSI as the lithium salt in electrolytes (Figure S8). Though the cathodic kinetics in LiFSI-based electrolytes are also worsened with increased discharge rate and decreased ESP, the deterioration rate is slower compared with LiTFSI-based electrolytes (Figure 2B). In detail, increasing the TTE content from 0 to 40% in electrolytes lowered $U_{Dis\text{-}lowest}$ by only 37 mV in LiFSI-based systems under 0.3 C, significantly less than the 174 mV drop in LiTFSI-based systems (Figures $2A_1$ and $2B_1$). Similarly, increasing the discharge rate from 0.1 to 0.5 C in 20% TTE electrolytes reduces $U_{Dis\text{-}lowest}$ by 150 mV in LiFSI-based systems, nearly half the reduction in LiTFSI-based systems (Figures $2A_2$ and $2B_2$). Worthy to be noted, the FSI^- in electrolytes can overcome the kinetic issues under concurrent low-ESP and high-rate conditions (the upper-right corner in Figure 2B). For the cells with 40% TTE electrolytes under 0.5 C, the LiFSI-based cells maintain a $U_{Dis\text{-}lowest}$ of 1.71 V above the discharge cut-off voltage and a specific capacity of 618 mAh g^{-1}, which is 3.47 times its LiTFSI-based counterparts (Figures S7 and S8). In brief, LiFSI efficiently reduces the cathodic polarization and enhances the cathodic kinetics, especially under harsh low-ESP and high-rate conditions.

To elucidate why FSI^- alleviates polarization in low-ESP electrolytes under high rates, the cathodic polarization versus the depth of discharge (DOD) is decoupled into ohmic, concentration, and activation polarizations (denoted as η_{ohm}, η_{con}, and η_{act}, respectively) in cells adopting 40% TTE electrolytes under 0.3, 0.4, and 0.5 C. Typically, η_{ohm}, η_{con}, and η_{act} are distinguished according to their time dependence on applied current and the Ohm's law according to the galvanostatic intermittent titration technique combining electrochemical impedance spectroscopy (GITT-EIS) method (detailed discussion in Figures S9–S11). In each cell with either LiTFSI- or LiFSI-based TTE electrolytes, the η_{ohm} takes up the smallest proportion of no more than 10%, and so manifesting ionic and electronic conductivity variation are not the primary cause of polarization deterioration (Figure S12). For η_{act} and η_{con} as the dominant polarizations, their values increase early in discharge, peak around the DOD of 0.3, and decrease thereafter until discharge termination (Figure S13). Therein, the DOD of 0.3 approximately corresponds to the point of the $U_{Dis\text{-}lowest}$ in the discharge curve and the point with the most concentrated LiPSs in electrolyte. Given the severe kinetic challenges at the DOD of 0.3, we focus on electrochemical behavior and dominant polarization analysis at this point.

To identify the dominant polarization causing the kinetic differences between LiTFSI- and LiFSI-based electrolytes, the η_{act} or η_{con} for the two electrolytes at identical discharge rates are compared (Figures 2C–2E). The values of η_{act} in LiFSI-based electrolytes are consistently smaller than those in LiTFSI-based TTE electrolytes, while the values of η_{con} show a minimal difference. Taking the discharge rate of 0.4 C as an example, the

Please cite this article in press as: Li et al., Competitive anion coordination overcomes charge-transfer barriers for lithium–sulfur batteries, Joule (2025), https://doi.org/10.1016/j.joule.2025.102259

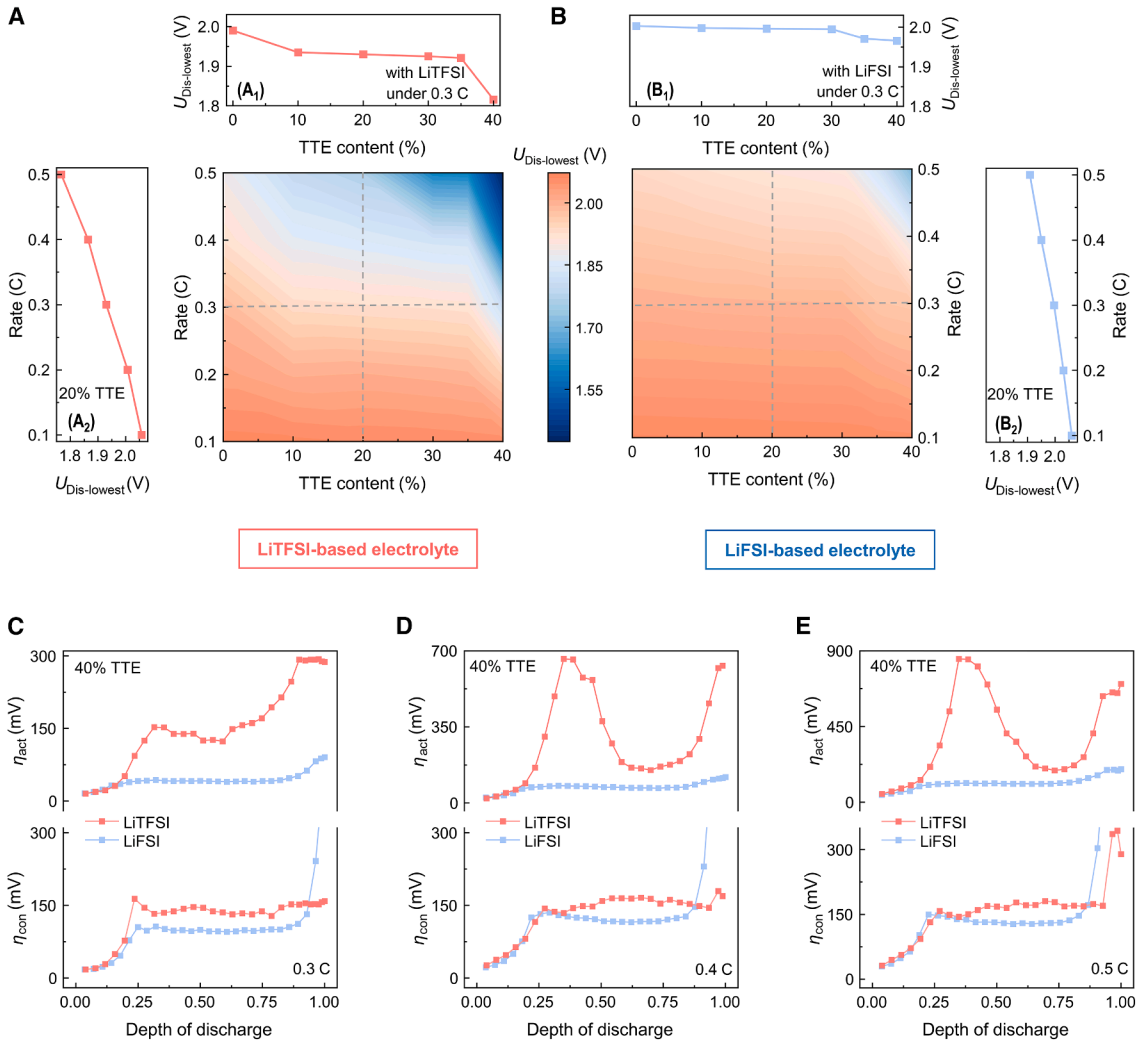

Figure 2. Polarization analysis of Li–S batteries with distinct anions

(A and B) Three-dimensional contour plots illustrating the $U_{Dis\text{-}lowest}$ as a function of discharge rate and TTE content in (A) LiTFSI-based and (B) LiFSI-based electrolytes. Dashed lines denote cross-sectional profiles at a fixed rate of 0.3 C (A_1 and B_1) or a fixed TTE content of 20% (A_2 and B_2).

(C–E) Activation polarization (η_{act}, upper) and concentration polarization (η_{con}, lower) of Li–S batteries employing LiTFSI- or LiFSI-based 40% TTE electrolytes under the rate of (C) 0.3 C, (D) 0.4 C, and (E) 0.5 C (cathode sulfur loading, 4.0 mg_S cm^{-2}).

values of η_{act} and η_{con} in LiFSI-based TTE electrolytes are 79.7 and 135 mV, respectively, which correspond to 12.0% and 93.7% of those (663 and 144 mV) in LiTFSI-based TTE electrolytes at the DOD of 0.3 (Figure 2D). At the DOD of 0.3, the ratios of η_{act} in LiFSI to η_{act} in LiTFSI are 28.5% and 13.2%, respectively, under 0.3 and 0.5 C, while the ratios of η_{con} in LiFSI to η_{con} in LiTFSI are 72.4% and 94.9%, respectively. Even under a higher TTE content of 50%, cells with LiFSI can still maintain smaller polarizations, especially η_{act}, than that with LiTFSI (Figures S14–S16). The significantly lowered η_{act} with minimal η_{con} change confirms that η_{act} instead of η_{con} is efficiently regulated in LiFSI-based TTE electrolytes. Since η_{act} reflects charge-transfer kinetic difficulty, FSI^- mainly optimizes the LiPS charge-transfer kinetics rather than mass-transport kinetics, thereby enhancing cathodic kinetics in electrolytes.

LiPS solvation structures in anion-competitive electrolytes

To disclose the mechanism of FSI^- in optimizing the LiPS charge-transfer kinetics, the LiPSs in solvated states and their solvation structures in electrolytes should be first clarified. In detail, the 40% TTE LiTFSI/LiFSI-based solutions with or without concentrated 2.0 $mol_{[S]}$ L^{-1} Li_2S_6 are adopted as the model electrolytes to investigate the solvated LiPSs.

Adding LiPSs to both LiTFSI-based and LiFSI-based electrolytes alter the electron densities around lithium and fluorine nuclei in salts, as revealed by ^7Li and ^{19}F nuclear magnetic resonance (NMR) spectroscopy analyses, confirming anion participation in the LiPS inner solvation shell (Figures S17–S19). In principle, both the TFSI and FSI anions coordinate with LiPSs via bidentate chelation following the lithium bond theory,[42] where

Please cite this article in press as: Li et al., Competitive anion coordination overcomes charge-transfer barriers for lithium–sulfur batteries, Joule (2025), https://doi.org/10.1016/j.joule.2025.102259

two oxygen atoms interact with a lithium atom in the LiPS molecule to form a stable six-membered-ring structure. Therefore, the negative charge distribution on these oxygen atoms determines the coordination capability. According to the electrostatic potential calculations, the electronegative region is dispersed more globally in FSI^- than in $TFSI^-$, and the natural bond orbital (NBO) charge of the oxygen atom is 40% larger in FSI^- than $TFSI^-$ (0.240 vs. 0.171 *e*) (Figures 3A and S20). The charge analysis results suggest that FSI^- has stronger LiPS coordination capability than $TFSI^-$ in theory.

In order to visualize anion participation in the LiPS inner solvation shell, molecular dynamics (MD) simulations are adopted in 40% TTE solutions with 1.0 mol L^{-1} LiTFSI or LiFSI and 2.0 $mol_{[S]}$ L^{-1} Li_2S_6, which are identical to the experimental composition for spectroscopies (Table S2). In the snapshot around LiPSs, three FSI^- directly interact with the Li_2S_6 molecule in the LiFSI-based electrolyte, while only one $TFSI^-$ directly interacts with Li_2S_6 in the LiTFSI-based electrolyte (Figure 3B). The different coordination numbers of anions in the LiPS inner solvation shell evidently illustrate that FSI^- is stronger in coordination capability than $TFSI^-$. Statistically, the radial distribution function $g(r)$ of anions centered on the polysulfide chain arises at $r = 3.7$ Å in LiFSI-based electrolytes, which is earlier than that at $r = 4.3$ Å in LiTFSI-based electrolytes (Figure 3C). Moreover, the strengthened peak intensity in the LiFSI-based electrolyte manifests that FSI^- interacts with LiPSs more tightly and exhibits more potential to enter the LiPS inner solvation shell. Additionally, the average coordination number in statistics of FSI^- is larger than that of $TFSI^-$ at the fixed radius centered on the polysulfide chain. For instance, the coordination number of FSI^- is 4.1-times larger than that of $TFSI^-$ (0.72 vs. 0.14) at $r = 6.0$ Å (which approximately corresponds to the LiPS inner solvation shell). To experimentally quantify the anion coordination percentage around LiPSs, fine Raman spectroscopies are adopted in the LiTFSI/LiFSI-based electrolytes with Li_2S_6, and the δ(SSSS) bending mode (the segment containing a four-sulfur-atom chain) in Li_2S_6 molecule, as well as the δ(S–N–S) bending mode in FSI^- or $TFSI^-$ are specially analyzed (Figures S21–S28). Though the anion coordination percentage rises along with the increment of TTE content, the coordination percentage of FSI^- is always larger than that of $TFSI^-$, whatever the TTE content is. Theoretical and experimental results conclusively demonstrate that FSI^- coordinates more strongly and numerously with LiPSs than $TFSI^-$ in low-ESP electrolytes.

Besides anion coordination, solvents in low-ESP electrolytes also participate in the LiPS inner solvation shell. To probe the TTE coordination capability with LiPSs, binding energies (E_b) between TTE and anion-coordinated Li_2S_6 (Li_2S_6-FSI^- or Li_2S_6-$TFSI^-$) are compared through density functional theory (DFT) calculations (Figures 3D and S29). In detail, the E_b between TTE and Li_2S_6-FSI^- is −0.99 eV, weaker than that of −1.16 eV between TTE and Li_2S_6-$TFSI^-$. The lower tendency of TTE binding with Li_2S_6-FSI^- than Li_2S_6-$TFSI^-$ illustrates that TTE is of weaker coordination capability to solvated LiPSs in LiFSI-based electrolytes than those in LiTFSI-based electrolytes. The ^{19}F-NMR spectroscopy results match well with the above TTE coordination tendency, where the peak shift of the fluorine atom in LiFSI-based electrolytes merely changes (by only 0.01 ppm) after the addition of Li_2S_6 (Figure S30). The little-altered ^{19}F peak shift manifests that TTE can hardly participate in the LiPS inner solvation shell in LiFSI-based electrolytes. To accurately demonstrate the TTE coordination difference between LiFSI- and LiTFSI-based electrolytes, ^{1}H-NMR diffusion ordered spectroscopy (DOSY) is conducted to detect the TTE diffusion coefficient (D_{TTE}) (Figures 3E and S31). In principle, the diffusion coefficient of coordinated solvent is smaller than that of free solvent, and its value will be further reduced if more solvents are in coordinated states. As a result, the D_{TTE} value in the LiFSI-based electrolyte with Li_2S_6 is 4.51×10^{-10} m^2 s^{-1}, which is slightly smaller than that without lithium salt and Li_2S_6 (5.38×10^{-10} m^2 s^{-1}), but apparently larger than that in the LiTFSI-based electrolytes with Li_2S_6 (2.48×10^{-10} m^2 s^{-1}) (Figure 3F). The above D_{TTE} differences illustrate that little TTE coordinates with LiPSs in LiFSI-based electrolytes, but more TTE coordinates with LiPSs in the LiTFSI-based electrolytes. Combining the DFT, ^{19}F-NMR, and ^{1}H-DOSY analyses, replacing $TFSI^-$ with FSI^- in low-ESP electrolytes significantly reduces both the number and strength of coordinating TTE.

Besides anions and TTE, DME coordination is non-negligible due to its strong solvating capability. To probe DME solvation with LiPSs, the E_b between DME and anion-coordinated Li_2S_6 (Li_2S_6-FSI^- or Li_2S_6-$TFSI^-$) is calculated (Figure S32). As a result, the E_b in the above two systems vary little (−1.22 vs. −1.23 eV), manifesting that the DME solvation capability is almost the same in LiFSI- or LiTFSI-based electrolytes in theory. Experimentally, to probe the DME coordination, ^{1}H-NMR spectroscopy of DME is conducted in LiFSI/LiTFSI-based electrolytes with or without Li_2S_6 (Figure 3G). After the addition of Li_2S_6, the DME peaks are downshifted in both LiFSI- and LiTFSI-based electrolytes, illustrating that more DME molecules coordinate with Li^+ and LiPSs. Moreover, the above downshift values exhibit little difference (0.07 vs. 0.09 ppm) between the two systems, suggesting that the DME coordination with LiPSs is similar in both strength and number. In brief, replacing $TFSI^-$ with FSI^- in low-ESP electrolytes does not alter DME solvation strength or number with LiPSs.

Considering the above analyses on LiPS solvation involving anions and solvents, we conclude anion and TTE coordination differs markedly between LiFSI- and LiTFSI-based electrolytes (Figure 3H). Concretely, DME strongly coordinates with LiPSs similarly in both systems. However, anions and TTE competitively coordinate with LiPSs, resulting in distinct solvation structures. In LiTFSI-based electrolytes, both $TFSI^-$ and TTE mediumly coordinate with LiPSs. Conversely, FSI^- exhibits much stronger competitive coordination capability than TTE, and the LiPS inner solvation shell contains more FSI^-. The significantly different LiPS solvation structures in anion-involved electrolytes directly impact LiPS charge-transfer kinetics and Li–S battery performances.

LiPS charge-transfer kinetics in anion-competitive electrolytes

The polarization decoupling results show superior LiPS charge-transfer kinetics in LiFSI-based electrolytes versus LiTFSI-based electrolytes, while spectroscopy and calculations reveal stronger competitive coordination of FSI^- over TTE and $TFSI^-$ in

Please cite this article in press as: Li et al., Competitive anion coordination overcomes charge-transfer barriers for lithium–sulfur batteries, Joule (2025), https://doi.org/10.1016/j.joule.2025.102259

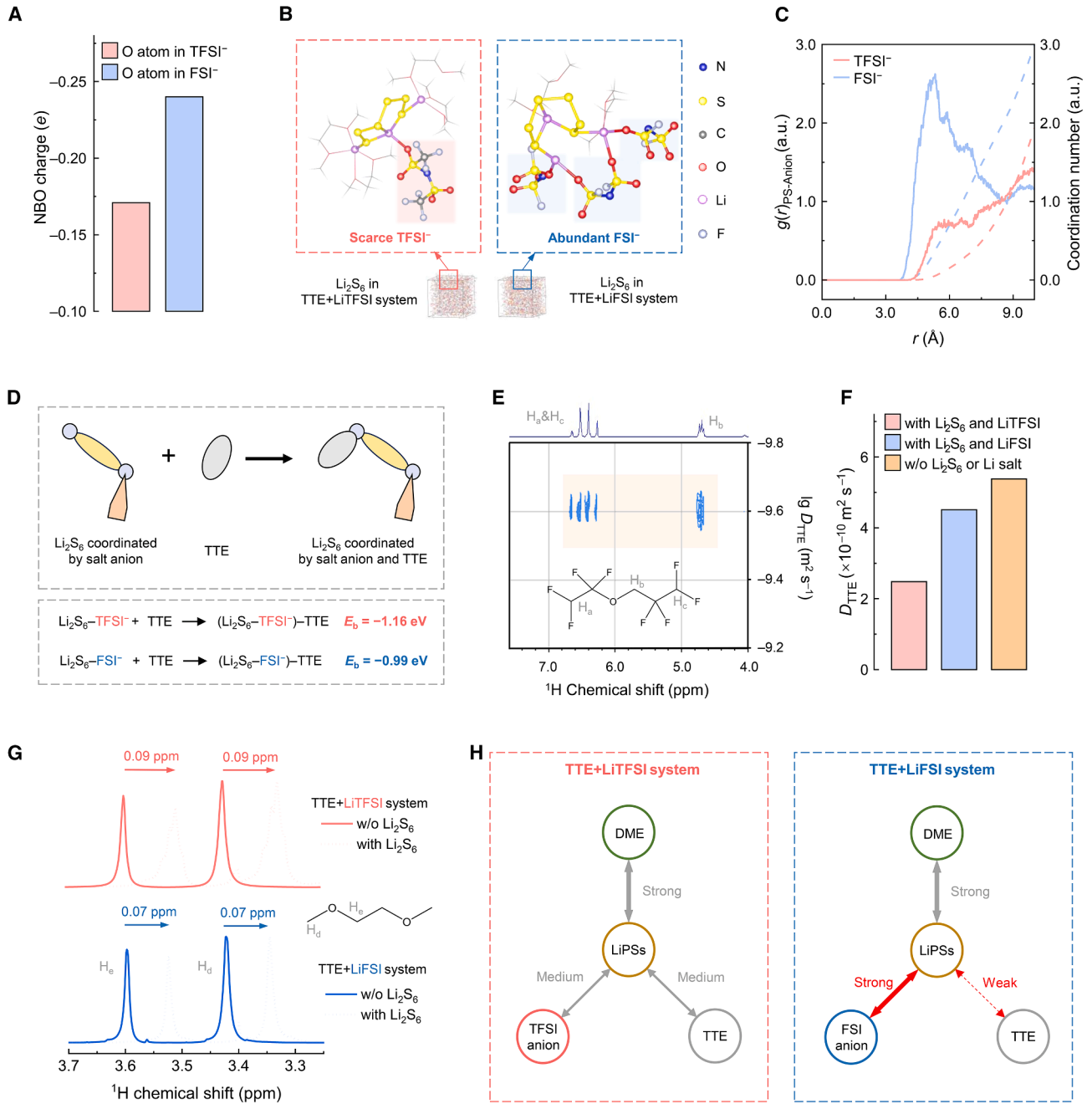

Figure 3. Identification of the anion-competitive LiPS solvation structure

(A) NBO charge analysis of the oxygen atom in $TFSI^-$ and FSI^-.

(B) MD simulation snapshots showing the coordination structures of Li_2S_6 in LiTFSI-based (left) and LiFSI-based (right) electrolytes.

(C) Radial distribution function $g(r)$ and coordination number of $TFSI^-$ and FSI^- around Li_2S_6 in electrolytes, where the radius r represents the distance between the barycenter of Li_2S_6 and the anion.

(D) Binding energy calculations for Li_2S_6-anion complexes interacting with TTE.

(E) Schematic illustration of ^{1}H-NMR DOSY experiments for TTE in electrolytes, where detailed H distributions in TTE molecules are labeled with H_a–H_c.

(F) Diffusion coefficients of TTE (D_{TTE}) in electrolytes with or without lithium salt.

(G) ^{1}H-NMR spectroscopy characterizing DME coordination in electrolytes, where detailed H distributions in DME molecules are labeled with H_d and H_e.

(H) Schematic diagram of the coordination capability between LiPSs and DME/TTE/anion in LiTFSI-based (left) and LiFSI-based (right) electrolytes.

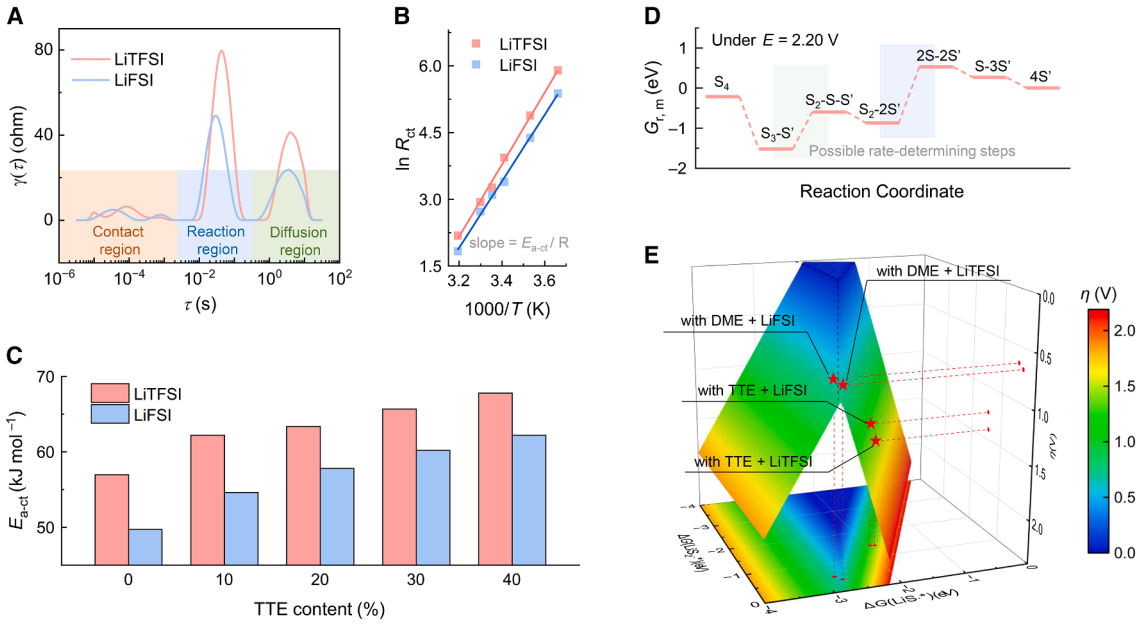

Figure 4. LiPS charge-transfer kinetics evaluation in anion-competitive electrolytes

(A) DRT analysis of Li_2S_6 symmetric cells with LiTFSI- and LiFSI-based electrolytes.

(B) Arrhenius fitting of charge-transfer activation energy ($E_{a\text{-}ct}$) through temperature-dependent EIS tests.

(C) $E_{a\text{-}ct}$ evolution in LiTFSI- and LiFSI-based electrolytes as TTE content increases.

(D) Schematic illustration of Gibbs free energy profile for LiPS reduction on graphene substrate at 2.20 V vs. Li/Li^+, where the species of Li_2S_4, $LiS_3\cdot$, $LiS_2\cdot$, $LiS\cdot$, and Li_2S are marked as S_4, S_3, S_2, S, and S' for convenience.

(E) Three-dimensional volcano plot of calculated overpotential vs. $\Delta G(LiS\cdot^*)$ and $\Delta G(LiS_2\cdot^*)$ for LiPS heterogeneous reactions.

the LiPS solvation structure. To disclose the microscopic mechanism of FSI^- in optimizing the LiPS charge-transfer kinetics, the LiPS intrinsic charge-transfer kinetics are correlated with their specific anion-involved LiPS solvation structure at the molecular level.

To evaluate the anion-involved LiPS charge-transfer kinetics of homogeneous reactions regarding the conversion between dissolved LiPSs, Li_2S_6 symmetric cells with LiTFSI- or LiFSI-based electrolytes with TTE content from 0% to 40% are adopted as the model system, and EIS tests are conducted under variable temperatures (T) from 273 to 313 K (Figures S33 and S34). To deconvolute the charge-transfer process in the Nyquist plots, distribution of relaxation time (DRT) analysis is performed. Three peaks can be observed at the characteristic time (τ) of c.a. 10^{-4}, 10^{-2}, and 10^{0} s, corresponding to the particle-contact, charge-transfer, and mass-transport processes in equivalent circuits (Figures 4A and S35). Therein, the charge-transfer resistance (R_{ct}) in the reaction region quantitatively indicates the difficulty of LiPS charge transfer in variable-ESP electrolytes. For instance, the R_{ct} in the LiFSI system is 37.2 Ω in the symmetric cells with 40% TTE electrolytes under room temperature, 21.4% smaller than that in the LiTFSI system. The reduced R_{ct} manifests that the charge-transfer kinetics in the LiFSI system are indeed superior in LiPS homogeneous reactions. Furthermore, the charge-transfer activation energy ($E_{a\text{-}ct}$) is fitted by plotting ln R_{ct} with $1/T$ according to the Arrhenius equation (Figures 4B and S36). The value of $E_{a\text{-}ct}$ is apparently enlarged from 57.0 to 67.8 kJ mol^{-1} in LiTFSI-based electrolytes and from 49.7 to 62.2 kJ mol^{-1} in LiFSI-based electrolytes as the TTE content increases from 0% to 40% (Figure 4C). Notably, the value of $E_{a\text{-}ct}$ in LiFSI-based electrolytes is smaller than that in LiTFSI-based electrolytes at each fixed TTE content. For instance, when the TTE content is 30%, the $E_{a\text{-}ct}$ is 60.2 kJ mol^{-1} in LiFSI-based electrolytes, which is 5.5 kJ mol^{-1} lower than that in LiTFSI-based electrolytes. The reduced $E_{a\text{-}ct}$ confirms LiFSI optimizes LiPS charge-transfer kinetics for homogeneous reactions in low-ESP electrolytes. Combined with solvation analysis, more FSI^- and less TTE coordination endows LiPSs with superior charge-transfer kinetics.

To probe the anion-involved LiPS charge-transfer kinetics of heterogeneous reactions regarding the conversion from dissolved LiPSs to solid Li_2S, DFT calculations on elemental reactions from Li_2S_4 to Li_2S are conducted (detailed discussion in the supplemental information).[43] Concretely, the optimized asymmetric reaction pathway comprise six single-electron-transfer steps:

$Li_2S_4 + (Li^+ + e^-) + * \rightarrow LiS_3\cdot^* + Li_2S$ (step I)

$Li_2S_4 + (Li^+ + e^-) + * \rightarrow LiS_3\cdot^* + Li_2S$ (step II)

$LiS_2\cdot^* + LiS\cdot^* + Li_2S + (Li^+ + e^-) \rightarrow LiS_2\cdot^* + 2Li_2S + *$ (step III)

$LiS_2\cdot^* + 2Li_2S + (Li^+ + e^-) + * \rightarrow 2LiS\cdot^* + 2Li_2S$ (step IV)

$2LiS\cdot^* + 2Li_2S + (Li^+ + e^-) \rightarrow LiS\cdot^* + 3Li_2S + *$ (step V)

$LiS\cdot^* + 3Li_2S + (Li^+ + e^-) \rightarrow 4Li_2S + *$ (step VI)

Therein, the * represents the reaction substrate (graphene is adopted here for interfacial reaction simulation), and radicals as well as Li_2S_4 molecules are calculated considering the explicit solvation model with two solvents and one salt coordination

Please cite this article in press as: Li et al., Competitive anion coordination overcomes charge-transfer barriers for lithium–sulfur batteries, Joule (2025), https://doi.org/10.1016/j.joule.2025.102259

(Figures S37–S40). In this way, the diagrams of Gibbs free energy evolution in the systems of DME + LiTFSI, DME + LiFSI, TTE + LiTFSI, and TTE + LiFSI can be calculated under the potential of 2.20 V (Figures 4D and S41). Note that the core elementary reaction in steps III, V, and VI is totally identical, and it corresponds to the consumption of LiS·* (i.e., LiS·* + ($Li^+ + e^-$) → Li_2S + *). Therefore, we only investigate the reactions in steps I–IV and probe the rate-determining step therein. Concretely, the energy barriers emerge in steps III and IV in the systems with DME coordination (i.e., DME + LiTFSI and DME + LiFSI), while the energy barriers emerge in steps II and IV in the systems with TTE coordination (i.e., TTE + LiTFSI and TTE + LiFSI). The variable positions of energy barriers demonstrate the significant alteration of polysulfide radical energy and reactivity after TTE coordination. When replacing DME coordination with TTE coordination around LiPSs, the energy barrier in the rate-determining step is severely enlarged (0.70 and 0.71 eV larger in LiFSI and LiTFSI systems, respectively), which illustrates that TTE coordination indeed hinders the intrinsic LiPS charge-transfer kinetics in heterogeneous reactions. Focusing on the anion coordination effect on the intrinsic LiPS redox kinetics, the energy barrier in the rate-determining step (step IV) is 0.69 eV for LiPSs coordinated by DME, and LiTFSI and is reduced to 0.60 eV (step III) for LiPSs coordinated by DME and LiFSI. The energy barrier for LiPSs coordinated by TTE and LiFSI is also lower than that by TTE and LiTFSI (1.30 vs. 1.40 eV). The reduced values manifest that LiFSI coordination lowers the charge-transfer energy barrier and accelerates the LiPS heterogeneous reaction kinetics.

To visualize the kinetic differences among the variable solvation structures, the overpotential of the LiPS heterogeneous reactions is calculated and displayed in the three-dimensional volcano plot versus ΔG(LiS·*) and ΔG(LiS_2·*) (Figure 4E). In detail, the overpotential of LiPSs coordinated by DME and LiFSI locates at region III, representing the rate-determining step is LiS· consumption, while the overpotentials of LiPSs coordinated by DME and LiTFSI, TTE and LiFSI, or TTE and LiTFSI locate at region IV, representing the rate-determining step is LiS_2· consumption (Figure S42). Notably, the calculated overpotential is aggravated after TTE coordination (0.91 and 1.03 times larger in LiFSI and LiTFSI systems, respectively) and lessened after LiFSI coordination (0.04 and 0.16 V smaller in DME and TTE systems, respectively). Due to the competitive coordination between TTE and anions on LiPSs mentioned before, the actual inner solvation shell for LiPSs in LiFSI-based electrolytes is abundant FSI^- and DME but scarce TTE, while it is abundant TTE and DME but scarce $TFSI^-$ for LiPSs in LiTFSI-based electrolytes (Figure S1). Consequently, the kinetic benefit of competitive LiFSI coordination and detriment of TTE coordination are respectively amplified and attenuated in LiFSI-based electrolytes, endowing LiPSs with significantly superior charge-transfer kinetics for heterogeneous reactions compared with LiTFSI-based electrolytes.

Li–S battery performances using anion-competitive electrolytes

Combined intrinsic kinetic analysis and solvation structure evaluation demonstrate that competitive coordination between anions and TTE significantly impacts LiPS charge-transfer kinetics. As a result, LiFSI-based electrolytes constitute an excellent approach to address sluggish kinetics induced by TTE addition. Regulating anion coordination enables practical Li–S batteries with both high energy density and long cycling lifespan, breaking the trade-off by avoiding cathodic kinetic disadvantages, while preserving anodic protective advantages of low-ESP electrolytes.

The feasibility of both smooth cathodic kinetics and promoted anodic stability is evaluated in coin cells assembled with high-sulfur-loading (4.0 mg_S cm^{-2}) cathodes and lean-excess anodes (50 μm in thickness). Under such harsh conditions, the cells with LiFSI-based electrolytes can still deliver an initial specific capacity of 1,139 mAh g^{-1} and stably operate for 180 cycles under a high rate of 0.3 C (Figure 5A). On the contrary, the cells with LiTFSI-based electrolytes exhibit a 64-cycle lifespan, only one-third of that of the cells with LiFSI-based electrolytes. The rapid loss in specific capacity of the 64th cycle can be ascribed to the cathodic polarization aggravation, where the voltage between the 1st and 2nd discharge plateaus reaches the cut-off voltage in the cells with LiTFSI-based electrolytes (Figure 5A, inset). For comparison, the discharge voltage keeps stable during cycling in the cells with LiFSI-based electrolytes, illustrating the superior LiPS cathodic kinetics induced by FSI^- coordination. If replacing TTE by DME to construct routine electrolytes, the Li–S cells under identical conditions cannot operate for over 30 cycles due to severe overcharge, underscoring the effectiveness of low-ESP electrolytes for anodic protection (Figure S43).

Cathodic kinetic enhancement via anion coordination is more pronounced in cells with ultrahigh-sulfur-loading cathodes (7.0 mg_S cm^{-2}) and lean-excess anodes (50 μm in thickness) tested under variable rates from 0.1 to 0.4 C (Figure S44). Quantitatively, the specific capacity drops sharply by 69.7% when the rate increases from 0.2 to 0.25 C in the cells with LiTFSI-based electrolytes, due to the enlarged cathodic polarizations, whereas the decrease is only 10.6% in the cells with LiFSI-based electrolytes (Figure S45). Additionally, the $U_{Dis\text{-}lowest}$ is consistently higher in LiFSI-based cells than LiTFSI-based cells under each rate (Figure 5B). For instance, the value of $U_{Dis\text{-}lowest}$ is 1.79 V in LiFSI-based electrolytes under a high rate of 0.4 C, while it is below the cut-off voltage of 1.7 V after the rate goes above 0.25 C in LiTFSI-based electrolytes. All the above increased specific capacity, lowered polarization, and improved rate-tolerance should be attributed to the enhanced LiPS charge-transfer kinetics by FSI^- coordination.

To probe the effectiveness of the anion coordination strategy in electrolytes with both smooth cathodic kinetics and preserved anodic protection, Ah-level Li–S pouch cells are assembled and evaluated. For the rate-testing pouch cells, besides adopting ultrahigh-sulfur-loading cathodes (around 7.5 mg_S cm^{-2}) and lean-excess anodes (75 μm in thickness), the electrolyte-to-sulfur (E/S) ratio is controlled as low as 3.5 g_{ele} g_S^{-1} (Table S4). The pouch cells with LiFSI-based electrolytes can stably operate at high rate of 0.35 C, significantly outperforming LiTFSI-based cells limited to 0.2 C (Figure 5C). The promoted high-rate tolerance under lean electrolyte conditions represents state-of-the-art performance in Ah-level Li–S pouch cells, surpassing previous reports typically limited to below 0.2 C (Figure 5D; Table S5). For stability testing, cell capacity is scaled to a 5-Ah

Please cite this article in press as: Li et al., Competitive anion coordination overcomes charge-transfer barriers for lithium–sulfur batteries, Joule (2025), https://doi.org/10.1016/j.joule.2025.102259

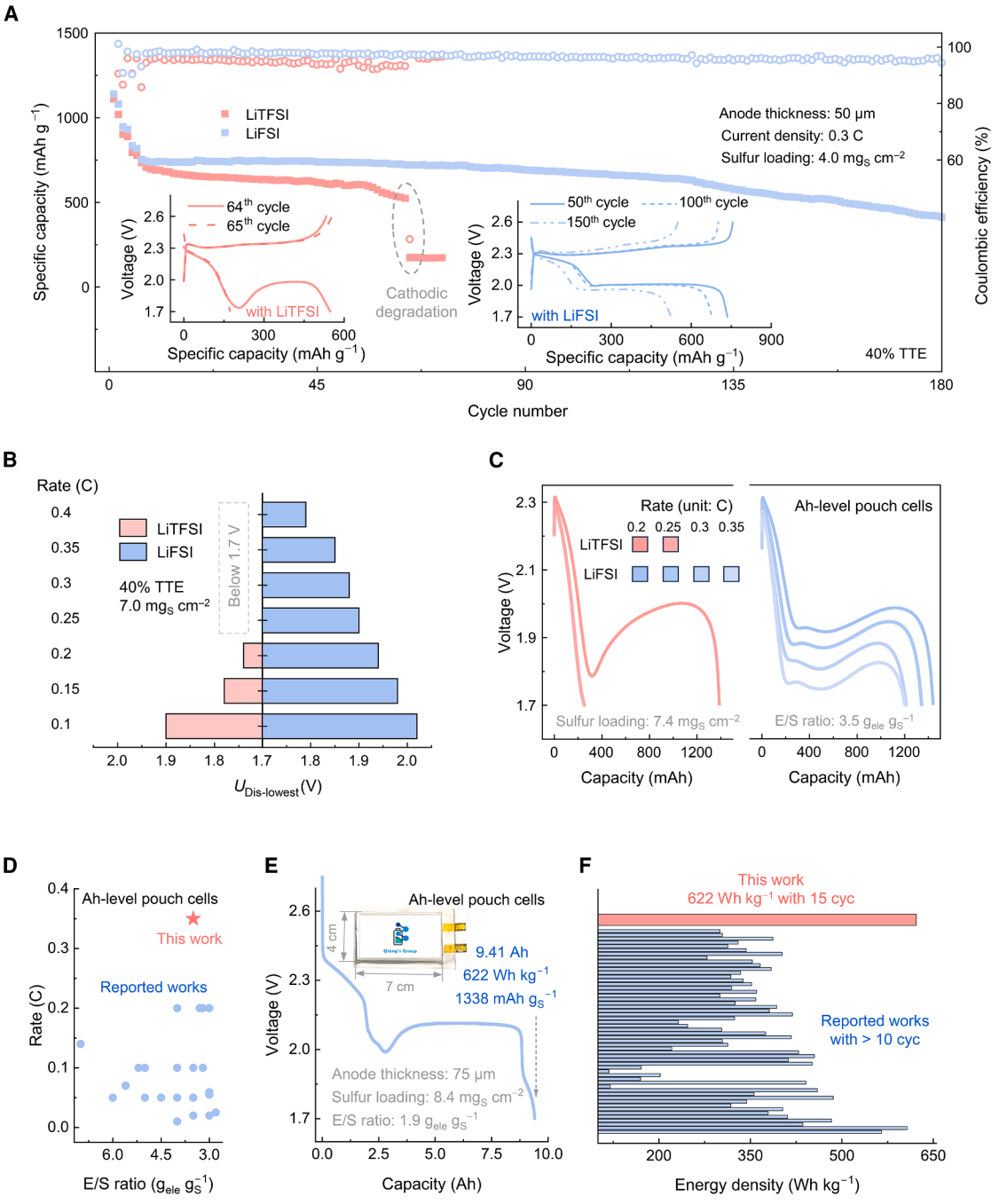

Figure 5. Li–S battery performances with anion-competitive electrolytes

(A) Cycling performances and corresponding charge-discharge profiles (inset) under high rates.

(B) $U_{Dis-lowest}$ comparisons in rate tests with ultrahigh-loading cathodes.

(C) Voltage profiles of Ah-level pouch cells under high rates from 0.2 to 0.35 C.

(D) Rate performance comparisons versus E/S ratio of Ah-level Li–S pouch cells between this work and previously reported works.

(E) Optical photograph (inset) and the 1st cycle profile of 10-Ah-level pouch cells. Note that the energy density of 622 Wh kg^{-1} is calculated based on the total mass of the pouch cell including package and tabs.

(F) Energy density comparison of Ah-level Li–S pouch cells between this work and previously reported works with over 10 cycles.

Please cite this article in press as: Li et al., Competitive anion coordination overcomes charge-transfer barriers for lithium–sulfur batteries, Joule (2025), https://doi.org/10.1016/j.joule.2025.102259

level to achieve higher actual energy density (Table S6). With anode-protective fluoroether and cathode-promoted anions, the pouch cells are endowed with 400 Wh kg^{-1} and 61 stable cycles (Figure S46). Moreover, the E/S ratio is reduced to 1.9 g_{ele} g_S^{-1} in 10-Ah-level pouch cells, and an ultrahigh energy density of 622 Wh kg^{-1} is yielded with 15 cycles (Figures 5E, S47, and S48). Note that the above energy densities are calculated based on total pouch cell mass including tabs and packages. Compared with reported works, pouch cells with LiFSI-based electrolytes excel in both energy density and cycling lifespan, demonstrating the full advantage of fluoroether anodic protection and FSI^- cathodic charge-transfer kinetic regulation (Figures 5F and S49; Table S7). Consequently, the competitive anion coordination strategy is efficient and applicable for practical pouch cells combining high energy density and prolonged cycling lifespan.

DISCUSSION

We pioneeringly disclose the anion-induced competitive solvation mechanism to promote the LiPS kinetics toward high-energy-density Li–S batteries. Anions contend against weakly solvating solvents for occupying the LiPS inner solvation shell and directly coordinating with LiPSs. Strengthening anion coordination and diminishing weakly solvating solvent coordination accelerates the LiPS redox kinetics in homogeneous and heterogeneous reactions, especially overcoming the charge-transfer barriers in low-ESP electrolytes. As a proof of concept, FSI^- coordination with enhanced competitive solvation capability reduces activation polarization and boosts cycling stability at high current densities. Ah-level pouch cells operate at high rates of 0.35 C and achieve an extraordinary energy density of 622 Wh kg^{-1} (based on total weight) with stable cycles, positioned as the state of the art in battery technology. By clarifying the anion-induced competitive solvation mechanism, our work challenges the conventional anion roles limited to ionic transport or interphase formation and establishes a paradigm shift in advancing Li–S batteries toward both high energy density and prolonged cycling lifespan.

METHODS

Raw materials

All the raw materials, including carbon nanotubes (CNTs), graphene (G), S_8, LiFSI, LiTFSI, lithium nitrate ($LiNO_3$), Li_2S, carbon paper (CP), sodium bis(trifluoromethanesulfonyl)imide (NaTFSI), sodium chloride (NaCl), deuterated chloroform ($CDCl_3$), DME, TTE, deionized (DI) water, poly(vinylidene fluoride) (PVDF, HSV-300), polypropylene (PP) separator (Celgard 2500), aluminum (Al) foil, copper (Cu) foil, and lithium (Li) foil were purchased from commercial sources and directly used without further purification.

Solution and electrolyte preparation

TTE solvent was mixed with DME solvent at certain volume ratios, dissolved 1.0 mol L^{-1} LiTFSI or LiFSI, and was adopted as LiTFSI-based or LiFSI-based TTE solutions, respectively. To prepare the LiTFSI/LiFSI-based TTE solutions with Li_2S_6, Li_2S and S_8 were mixed in the TTE solutions with a molar ratio of 8:5 and stirred at room temperature. The Li_2S_6 concentration was set to be 2.0 $mol_{[S]}$ L^{-1}. Spectroscopic experiments including DN measurements, NMR, and Raman spectroscopy tests, and electrochemical tests including shuttle current tests, Coulombic efficiency measurements, and symmetric cell evaluations were based on the LiTFSI/LiFSI-based TTE solutions and LiTFSI/LiFSI-based TTE solutions with Li_2S_6. Additional 2.0 wt % $LiNO_3$ dissolved in LiTFSI/LiFSI-based TTE solutions were adopted as the LiTFSI/LiFSI-based TTE electrolytes. Experiments including cycling performance evaluations and galvanostatic tests in Li–S full cells were based on the LiTFSI/LiFSI-based TTE electrolytes.

Spectroscopic experiments

The ^{23}Na NMR spectra were recorded on a JNM-ECZ400 NMR spectrometer to measure the DN. Concretely, the NMR tubes were coaxial types, where 10 mmol L^{-1} NaCl aqueous solution as the internal reference was filled in the inner tube, and the targeted solutions were filled in the outer tube. ^7Li-NMR spectra were recorded on the same NMR spectrometer to detect the LiPS surrounding environments in solutions. In detail, the NMR tubes were coaxial types, where pure $CDCl_3$ solvents as the deuterated reagents were filled in the inner tube to lock the field, and the TTE solutions were filled in the outer tube. For the DOSY tests, the diffusion coefficient of TTE solvent molecules were measured by using ^1H pulsed field gradient NMR at Larmor frequencies on a 700 MHz NMR spectrometer (Bruker Avance III HD 700 MHz). The echo heights, $I(G)$, obtained as a function of gradient strength (G) using bipolar gradients with convection compensate gradients were fitted with the Stejskal-Tanner equation as follows:

$$\boldsymbol{I}(G) = I_0 \times \exp\left(-\boldsymbol{D} \times (\gamma \boldsymbol{G}\delta)^2 \times \left(\Delta - \frac{\delta}{3}\right)\right)$$

Therein, $I(G)$ and I_0 are the echo height with the gradient strength of G and 0, respectively; D is the diffusion coefficient; and γ is the gyromagnetic ratio for the ^1H nuclei. The gradient strength G and duration (δ) of gradient pulse and the distance between the two gradients (Δ) were properly chosen for a sufficient decay of the echo height based upon the nuclei observed and diffusion coefficient. For the Raman spectra tests, the TTE solutions with Li_2S_6 were filled into a quartz glass cuvette and the spectra were recorded with 532-nm He-Ne laser in a Horiba Jobin Yvon LabRAM HR800 Raman spectrometer.

Further details regarding the methods can be found in the supplemental methods.

RESOURCE AVAILABILITY

Lead contact

Requests for further information and resources should be directed to and will be fulfilled by the lead contact, Qiang Zhang (zhang-qiang@mails.tsinghua.edu.cn).

Materials availability

This study did not generate new unique reagents.

Data and code availability

This paper does not report original code. All data reported in this paper will be shared by the lead contact upon request.

ACKNOWLEDGMENTS

This work was supported by the National Key Research and Development Program (2024YFE0209500), the Beijing Municipal Natural Science Foundation (L247015 and L233004), National Natural Science Foundation of China (T2322015, 22393900, 52394170, 22109086, 22209010, 224B2913, and 22409116), Xplorer Prize, and Tsinghua University Initiative Scientific Research Program. The authors acknowledged the support from Tsinghua National Laboratory for Information Science and Technology for theoretical simulations. We thank Zheng Li, Zi-Xian Chen, Dr. Chang-Xin Zhao, and Dr. Xue-Qiang Zhang for the helpful discussions.

AUTHOR CONTRIBUTIONS

X.-Y.L., B.-Q.L., and Q.Z. conceived the idea for the project. X.-Y.L., T.J., and M.Z. performed electrochemical and spectroscopic experiments. S.F., Y.-C.G., and X.C. conducted the theoretical simulations. X.-Y.L., B.-Q.L., J.-Q.H., and Q.Z. drafted the paper. B.-Q.L. and Q.Z. directed the project.

DECLARATION OF INTERESTS

The authors declare no competing interests.

SUPPLEMENTAL INFORMATION

Supplemental information can be found online at https://doi.org/10.1016/j.joule.2025.102259.

Received: August 29, 2025
Revised: October 24, 2025
Accepted: November 17, 2025

REFERENCES

1. Wang, C.-Y., Liu, T., Yang, X.-G., Ge, S., Stanley, N.V., Rountree, E.S., Leng, Y., and McCarthy, B.D. (2022). Fast charging of energy-dense lithium-ion batteries. Nature *611*, 485–490. https://doi.org/10.1038/s41586-022-05281-0.
2. Meng, Y.S., Srinivasan, V., and Xu, K. (2022). Designing better electrolytes. Science *378*, eabq3750. https://doi.org/10.1126/science.abq3750.
3. Pang, Q., Meng, J., Gupta, S., Hong, X., Kwok, C.Y., Zhao, J., Jin, Y., Xu, L., Karahan, O., Wang, Z., et al. (2022). Fast-charging aluminium–chalcogen batteries resistant to dendritic shorting. Nature *608*, 704–711. https://doi.org/10.1038/s41586-022-04983-9.
4. Li, X.-Y., Feng, S., Zhao, C.-X., Cheng, Q., Chen, Z.-X., Sun, S.-Y., Chen, X., Zhang, X.-Q., Li, B.-Q., Huang, J.-Q., et al. (2022). Regulating lithium salt to inhibit surface gelation on an electrocatalyst for high-energy-density lithium–sulfur batteries. J. Am. Chem. Soc. *144*, 14638–14646. https://doi.org/10.1021/jacs.2c04176.
5. Lei, J., Zhang, Y., Yao, Y., Shi, Y., Leung, K.L., Fan, J., and Lu, Y.-C. (2023). An active and durable molecular catalyst for aqueous polysulfide-based redox flow batteries. Nat. Energy *8*, 1355–1364. https://doi.org/10.1038/s41560-023-01370-0.
6. Xu, J., Zhang, J., Pollard, T.P., Li, Q., Tan, S., Hou, S., Wan, H., Chen, F., He, H., Hu, E., et al. (2023). Electrolyte design for Li-ion batteries under extreme operating conditions. Nature *614*, 694–700. https://doi.org/10.1038/s41586-022-05627-8.
7. Gao, Y.-C., Yuan, Y.-H., Huang, S., Yao, N., Yu, L., Chen, Y.-P., Zhang, Q., and Chen, X. (2025). A knowledge–data dual-driven framework for predicting the molecular properties of rechargeable battery electrolytes. Angew. Chem. Int. Ed. *64*, e202416506. https://doi.org/10.1002/anie.202416506.
8. Yang, Y., Biswas, S., Xu, R., Xiao, X., Xu, X., Zhang, P., Gong, H., Zheng, X., Peng, Y., Li, J., et al. (2024). Capacity recovery by transient voltage pulse in silicon-anode batteries. Science *386*, 322–327. https://doi.org/10.1126/science.adn1749.
9. Lu, D., Li, R., Rahman, M.M., Yu, P., Lv, L., Yang, S., Huang, Y., Sun, C., Zhang, S., Zhang, H., et al. (2024). Ligand-channel-enabled ultrafast Li-ion conduction. Nature *627*, 101–107. https://doi.org/10.1038/s41586-024-07045-4.
10. Dong, H., Tutusaus, O., Liang, Y., Zhang, Y., Lebens-Higgins, Z., Yang, W., Mohtadi, R., and Yao, Y. (2020). High-power Mg batteries enabled by heterogeneous enolization redox chemistry and weakly coordinating electrolytes. Nat. Energy *5*, 1043–1050. https://doi.org/10.1038/s41560-020-00734-0.
11. Yao, Y.-X., Xu, L., Yan, C., and Zhang, Q. (2025). Principles and trends in extreme fast charging lithium-ion batteries. EES Batteries *1*, 9–22. https://doi.org/10.1039/D4EB00011K.
12. Yang, Y., Yang, W., Yang, H., and Zhou, H. (2023). Electrolyte design principles for low-temperature lithium-ion batteries. eScience *3*, 100170. https://doi.org/10.1016/j.esci.2023.100170.
13. Suo, L., Borodin, O., Gao, T., Olguin, M., Ho, J., Fan, X., Luo, C., Wang, C., and Xu, K. (2015). "Water-in-salt" electrolyte enables high-voltage aqueous lithium-ion chemistries. Science *350*, 938–943. https://doi.org/10.1126/science.aab1595.
14. Zheng, X., Cao, Z., Luo, W., Weng, S., Zhang, X., Wang, D., Zhu, Z., Du, H., Wang, X., Qie, L., et al. (2023). Solvation and interfacial engineering enable −40°C operation of graphite/NCM batteries at energy density over 270 Wh kg^{-1}. Adv. Mater. *35*, 2210115. https://doi.org/10.1002/adma.202210115.
15. Yao, Y.-X., Chen, X., Yao, N., Gao, J.-H., Xu, G., Ding, J.-F., Song, C.-L., Cai, W.-L., Yan, C., and Zhang, Q. (2023). Unlocking charge transfer limitations for extreme fast charging of Li-ion batteries. Angew. Chem. Int. Ed. *62*, e202214828. https://doi.org/10.1002/anie.202214828.
16. Song, Y.-W., Shen, L., Yao, N., Feng, S., Cheng, Q., Ma, J., Chen, X., Li, B.-Q., and Zhang, Q. (2024). Anion-involved solvation structure of lithium polysulfides in lithium–sulfur batteries. Angew. Chem. Int. Ed. *63*, e202400343. https://doi.org/10.1002/anie.202400343.
17. Chen, Z.-X., Cheng, Q., Li, X.-Y., Li, Z., Song, Y.-W., Sun, F., Zhao, M., Zhang, X.-Q., Li, B.-Q., and Huang, J.-Q. (2023). Cathode kinetics evaluation in lean-electrolyte lithium–sulfur batteries. J. Am. Chem. Soc. *145*, 16449–16457. https://doi.org/10.1021/jacs.3c02786.
18. Kwak, W.-J., Rosy, Sharon, D., Xia, C., Kim, H., Johnson, L.R., Bruce, P.G., Nazar, L.F., Sun, Y.-K., Frimer, A.A., et al. (2020). Lithium–oxygen batteries and related systems: Potential, status, and future. Chem. Rev. *120*, 6626–6683. https://doi.org/10.1021/acs.chemrev.9b00609.
19. Cheng, Q., Chen, Z.-X., Li, X.-Y., Hou, L.-P., Bi, C.-X., Zhang, X.-Q., Huang, J.-Q., and Li, B.-Q. (2023). Constructing a 700 Wh kg^{-1}-level rechargeable lithium–sulfur pouch cell. J. Energy Chem. *76*, 181–186. https://doi.org/10.1016/j.jechem.2022.09.029.
20. Chu, H., Noh, H., Kim, Y.-J., Yuk, S., Lee, J.-H., Lee, J., Kwack, H., Kim, Y., Yang, D.-K., and Kim, H.-T. (2019). Achieving three-dimensional lithium sulfide growth in lithium-sulfur batteries using high-donor-number anions. Nat. Commun. *10*, 188. https://doi.org/10.1038/s41467-018-07975-4.
21. Wang, Q., Zhao, C., Wang, J., Yao, Z., Wang, S., Kumar, S.G.H., Ganapathy, S., Eustace, S., Bai, X., Li, B., et al. (2023). High entropy liquid electrolytes for lithium batteries. Nat. Commun. *14*, 440. https://doi.org/10.1038/s41467-023-36075-1.
22. Zhou, J., Holekevi Chandrappa, M.L., Tan, S., Wang, S., Wu, C., Nguyen, H., Wang, C., Liu, H., Yu, S., Miller, Q.R.S., et al. (2024). Healable and conductive sulfur iodide for solid-state Li–S batteries. Nature *627*, 301–305. https://doi.org/10.1038/s41586-024-07101-z.
23. Han, Z., Gao, R., Wang, T., Tao, S., Jia, Y., Lao, Z., Zhang, M., Zhou, J., Li, C., Piao, Z., et al. (2023). Machine-learning-assisted design of a binary descriptor to decipher electronic and structural effects on sulfur reduction kinetics. Nat. Catal. *6*, 1073–1086. https://doi.org/10.1038/s41929-023-01041-z.

24. Li, X.-Y., Zhao, M., Song, Y.-W., Bi, C.-X., Li, Z., Chen, Z.-X., Zhang, X.-Q., Li, B.-Q., and Huang, J.-Q. (2025). Polysulfide chemistry in metal–sulfur batteries. Chem. Soc. Rev. *54*, 4822–4873. https://doi.org/10.1039/D4CS00318G.

25. Lee, J., Zhou, S., Ferrari, V.C., Zhao, C., Sun, A., Nicholas, S., Liu, Y., Sun, C., Wierzbicki, D., Parkinson, D.Y., et al. (2025). Halide segregation to boost all-solid-state lithium-chalcogen batteries. Science *388*, 724–729. https://doi.org/10.1126/science.adt1882.

26. Liu, R., Wei, Z., Peng, L., Zhang, L., Zohar, A., Schoeppner, R., Wang, P., Wan, C., Zhu, D., Liu, H., et al. (2024). Establishing reaction networks in the 16-electron sulfur reduction reaction. Nature *626*, 98–104. https://doi.org/10.1038/s41586-023-06918-4.

27. Zhao, M., Peng, H.-J., Li, B.-Q., and Huang, J.-Q. (2024). Kinetic promoters for sulfur cathodes in lithium–sulfur batteries. Acc. Chem. Res. *57*, 545–557. https://doi.org/10.1021/acs.accounts.3c00698.

28. Hua, W., Shang, T., Li, H., Sun, Y., Guo, Y., Xia, J., Geng, C., Hu, Z., Peng, L., Han, Z., et al. (2023). Optimizing the p charge of S in p-block metal sulfides for sulfur reduction electrocatalysis. Nat. Catal. *6*, 174–184. https://doi.org/10.1038/s41929-023-00912-9.

29. Song, Y.-W., Shen, L., Li, X.-Y., Zhao, C.-X., Zhou, J., Li, B.-Q., Huang, J.-Q., and Zhang, Q. (2024). Phase equilibrium thermodynamics of lithium–sulfur batteries. Nat. Chem. Eng. *1*, 588–596. https://doi.org/10.1038/s44286-024-00115-4.

30. Song, H., Münch, K., Liu, X., Shen, K., Zhang, R., Weintraut, T., Yusim, Y., Jiang, D., Hong, X., Meng, J., et al. (2025). All-solid-state Li–S batteries with fast solid–solid sulfur reaction. Nature *637*, 846–853. https://doi.org/10.1038/s41586-024-08298-9.

31. Zhao, M., Li, X.-Y., Chen, X., Li, B.-Q., Kaskel, S., Zhang, Q., and Huang, J.-Q. (2021). Promoting the sulfur redox kinetics by mixed organodiselenides in high-energy-density lithium–sulfur batteries. eScience *1*, 44–52. https://doi.org/10.1016/j.esci.2021.08.001.

32. Chen, Z.-X., Zhao, J.-J., Fang, G.-Y., Sun, F., Zhao, M., Zhang, X.-Q., Li, B.-Q., and Huang, J.-Q. (2025). Sufficient cathode infiltration for stable 500 Wh kg^{-1} level lithium–sulfur batteries. J. Energy Chem. *109*, 129–137. https://doi.org/10.1016/j.jechem.2025.05.006.

33. Zhao, C.-X., Li, X.-Y., Han, H., Feng, Y., Tang, C., Li, X., Zhang, L., Stern, C. L., Zhang, Q., and Stoddart, J.F. (2024). Analytical noncovalent electrochemistry for battery engineering. Nat. Chem. Eng. *1*, 251–260. https://doi.org/10.1038/s44286-024-00038-0.

34. Shyamsunder, A., Beichel, W., Klose, P., Pang, Q., Scherer, H., Hoffmann, A., Murphy, G.K., Krossing, I., and Nazar, L.F. (2017). Inhibiting polysulfide shuttle in lithium–sulfur batteries through low-ion-pairing salts and a triflamide solvent. Angew. Chem. Int. Ed. *56*, 6192–6197. https://doi.org/10.1002/anie.201701026.

35. Liu, Y., Xu, L., Yu, Y., He, M., Zhang, H., Tang, Y., Xiong, F., Gao, S., Li, A., Wang, J., et al. (2023). Stabilized Li–S batteries with anti-solvent-tamed quasi-solid-state reaction. Joule *7*, 2074–2091. https://doi.org/10.1016/j.joule.2023.07.013.

36. Li, X.-Y., Li, B.-Q., Feng, S., Li, Z., Shen, L., Sun, S.-Y., Chen, Z.-X., Jin, T., Chen, X., Zhao, M., et al. (2025). Two-stage solvation of lithium polysulfides in working lithium–sulfur batteries. J. Am. Chem. Soc. *147*, 15435–15447. https://doi.org/10.1021/jacs.5c01588.

37. Su, C.-C., He, M., Amine, R., and Amine, K. (2019). A selection rule for hydrofluoroether electrolyte cosolvent: establishing a linear free-energy relationship in lithium–sulfur batteries. Angew. Chem. Int. Ed. *58*, 10591–10595. https://doi.org/10.1002/anie.201904240.

38. Kim, S.C., Gao, X., Liao, S.-L., Su, H., Chen, Y., Zhang, W., Greenburg, L. C., Pan, J.-A., Zheng, X., Ye, Y., et al. (2024). Solvation-property relationship of lithium–sulphur battery electrolytes. Nat. Commun. *15*, 1268. https://doi.org/10.1038/s41467-023-44527-x.

39. Li, X.-Y., Feng, S., Song, Y.-W., Zhao, C.-X., Li, Z., Chen, Z.-X., Cheng, Q., Chen, X., Zhang, X.-Q., Li, B.-Q., et al. (2024). Kinetic evaluation on lithium polysulfide in weakly solvating electrolyte toward practical lithium–sulfur batteries. J. Am. Chem. Soc. *146*, 14754–14764. https://doi.org/10.1021/jacs.4c02603.

40. Weller, C., Pampel, J., Dörfler, S., Althues, H., and Kaskel, S. (2019). Polysulfide shuttle suppression by electrolytes with low density for high-energy lithium–sulfur batteries. Energy Technol. *7*, 1900625. https://doi.org/10.1002/ente.201900625.

41. Gao, X., Yu, Z., Wang, J., Zheng, X., Ye, Y., Gong, H., Xiao, X., Yang, Y., Chen, Y., Bone, S.E., et al. (2023). Electrolytes with moderate lithium polysulfide solubility for high-performance long-calendar-life lithium–sulfur batteries. Proc. Natl. Acad. Sci. USA *120*, e2301260120. https://doi.org/10.1073/pnas.2301260120.

42. Yao, N., Chen, X., Sun, S.-Y., Gao, Y.-C., Yu, L., Gao, Y.-B., Li, W.-L., and Zhang, Q. (2025). Identifying the lithium bond and lithium ionic bond in electrolytes. Chem *11*, 102254. https://doi.org/10.1016/j.chempr.2024.07.016.

43. Feng, S., Fu, Z.-H., Chen, X., Li, B.-Q., Peng, H.-J., Yao, N., Shen, X., Yu, L., Gao, Y.-C., Zhang, R., et al. (2022). An electrocatalytic model of the sulfur reduction reaction in lithium–sulfur batteries. Angew. Chem. Int. Ed. *61*, e202211448. https://doi.org/10.1002/anie.202211448.